

# Computational study of inertial migration of prolate particles in a straight rectangular channel

Cite as: Phys. Fluids **34**, 082021 (2022); <https://doi.org/10.1063/5.0100963>

Submitted: 27 May 2022 • Accepted: 27 July 2022 • Accepted Manuscript Online: 28 July 2022 • Published Online: 19 August 2022

 Giuseppe Lauricella,  Jian Zhou (周剑),  Qiyue Luan (栾绮月), et al.

## COLLECTIONS

 This paper was selected as Featured



View Online



Export Citation



CrossMark

## ARTICLES YOU MAY BE INTERESTED IN

[Numerical simulations of cell sorting through inertial microfluidics](#)

Phys. Fluids **34**, 072009 (2022); <https://doi.org/10.1063/5.0096543>

[Microfluidic techniques for isolation, formation, and characterization of circulating tumor cells and clusters](#)

APL Bioengineering **6**, 031501 (2022); <https://doi.org/10.1063/5.0093806>

[Two-stage fourth-order subcell finite volume method on hexahedral meshes for compressible flows](#)

Phys. Fluids **34**, 086110 (2022); <https://doi.org/10.1063/5.0102640>

APL Machine Learning

Open, quality research for the networking communities

**Now Open for Submissions**

LEARN MORE



# Computational study of inertial migration of prolate particles in a straight rectangular channel

Cite as: Phys. Fluids **34**, 082021 (2022); doi: 10.1063/5.0100963

Submitted: 27 May 2022 · Accepted: 27 July 2022 ·

Published Online: 19 August 2022



View Online



Export Citation



CrossMark

Giuseppe Lauricella,  Jian Zhou (周剑),  Qiyue Luan (栾绮月),  Ian Papautsky,  and Zhangli Peng (彭张立)<sup>a)</sup> 

## AFFILIATIONS

Department of Biomedical Engineering, University of Illinois Chicago, Chicago, Illinois 60607, USA

<sup>a)</sup> Author to whom correspondence should be addressed: [zhpeng@uic.edu](mailto:zhpeng@uic.edu)

## ABSTRACT

Inertial migration of spherical particles has been investigated extensively using experiments, theory, and computational modeling. Yet, a systematic investigation of the effect of particle shape on inertial migration is still lacking. Herein, we numerically mapped the migration dynamics of a prolate particle in a straight rectangular microchannel using smoothed particle hydrodynamics at moderate Reynolds number flows. After validation, we applied our model to 2:1 and 3:1 shape aspect ratio particles at multiple confinement ratios. Their effects on the final focusing position, rotational behavior, and transitional dynamics were studied. In addition to the commonly reported tumbling motion, for the first time, we identified a new logrolling behavior of a prolate ellipsoidal particle in the confined channel. This new behavior occurs when the confinement ratio is above an approximate threshold value of  $K=0.72$ . Our microfluidic experiments using cell aggregates with similar shape aspect ratio and confinement ratio confirmed this new predicted logrolling motion. We also found that the same particle can undergo different rotational modes, including kayaking behavior, depending on its initial cross-sectional position and orientation. Furthermore, we examined the migration speed, angular velocity, and rotation period as well as their dependence on both particle shape aspect ratio and confinement ratio. Our findings are especially relevant to the applications where particle shape and alignment are used for sorting and analysis, such as the use of barcoded particles for biochemical assays through optical reading, or the shape-based enrichment of microalgae, bacteria, and chromosomes.

Published under an exclusive license by AIP Publishing. <https://doi.org/10.1063/5.0100963>

## I. INTRODUCTION

In the past decade, inertial microfluidics has gained popularity among the different techniques to separate and sort cells and particles at the microscale.<sup>1</sup> It is particularly suitable for biological and medical applications since it solely relies on the effect of fluid inertia.<sup>2,3</sup> Many microfluidic devices employ external forces using either an electromagnetic field,<sup>4–6</sup> acoustic field,<sup>7,8</sup> or light field<sup>9,10</sup> that could result in damage to the biological particles that are being analyzed. There are also a variety of passive microfluidics techniques that exploit hydrodynamic forces, such as hydrodynamic filtration (HDF), deterministic lateral displacement (DLD), pinched-flow fractionation (PFF), and gravitational methods.<sup>11,12</sup>

However, most of these methods are limited by their low throughput and design complexity, thus hindering industrial-scale application.<sup>13</sup> Inertial microfluidics exploits fluid inertia in confined channel flows, where the Reynolds number (the ratio between inertial and viscous forces in a flow) is typically in the range of 1–100, and the

laminar flow regime is ensured. In a straight channel with either a square or a rectangular cross-section, particles are subjected to inertial lift forces. When the forces are balanced, a stable equilibrium position for a particle can be achieved.<sup>14</sup> The current understanding of the underlying physics of this phenomenon is based on the two main forces acting on a spherical particle—the shear gradient-induced lift force and the wall-induced lift force.<sup>15</sup> In addition to these, in specific cases, such as spiral channels, other secondary lift forces take place and further influence the final equilibrium position of the particle. In general, several variables affect the inertial migration of a particle. These include flow parameters, types of channel cross-sections and geometries, and particle and suspension characteristics. In a rectangular cross-section, there are typically two stable equilibrium positions located close to the longer channel walls, at the center mid-line.

The majority of studies on inertial migration have focused on spherical particles, and there is a lack of experimental and computational studies on shaped particles due to the associated technical

challenges. Shaped particles are difficult to manufacture, and their complex dynamics make their simulations computationally expensive. Common non-spherical particles include ellipsoids, such as prolate ( $\lambda = \text{radial diameter/equatorial diameter} > 1$ ) and oblate ( $\lambda < 1$ ); non-ellipsoids, such as rod-like and disk-shaped beads; and asymmetric particles. Cells found in biological samples are best represented by deformable spherical particles, capable of changing their morphology, and thus, shape could be used to distinguish between different cell types, cell states, and cell cycle stages,<sup>13</sup> but also between cells and bacteria, that are generally non-spherical.<sup>16</sup> The first theoretical study on ellipsoids was done by Jeffery in 1922,<sup>17</sup> considering a simple shear flow in Stokes regime ( $Re=0$ ). He showed that the particles rotate around their vorticity axis, which is perpendicular to the plane of the flow gradient, as shown in Fig. 1(a). He found that a particle can undergo a set of infinite possible orbits that depend on the starting orientation, the so-called Jeffery orbits, which include kayaking, tumbling, and logrolling [Figs. 1(b)–1(d)]. He also studied the particle angular velocity and provided a formula to compute its orbit period given the aspect ratio and the shear rate. Despite a significant number of studies of ellipsoidal particles in shear flows,<sup>18</sup> there is little work on the rotational and inertial behaviors of ellipsoidal particles in microchannels. For a non-spherical particle in a microfluidic system, the lateral migration and the rotation are strongly related, and the experimental observation of exact motion is not trivial and requires new imaging techniques such as 3D reconstruction. It has been shown that in a Poiseuille flow a prolate particle prefers to tumble,<sup>19,20</sup> similar to the studies in shear flows. The main experimental work reported in the literature on the study of the shape effects on the lateral migration and translational behavior is the one by Di Carlo and his co-workers.<sup>13,21</sup> Hur *et al.*<sup>21</sup> experimentally investigated the lateral and vertical equilibrium positions of a variety of artificial beads, with different sizes

and cross-sectional shapes. From the numerical side, the complex rotational behavior of non-spherical particles is associated with a smaller time step and requires a higher computational cost.<sup>22</sup> Lashgari *et al.*<sup>23</sup> mapped the inertial migration dynamics of oblate particles in square and rectangular microchannels. To the best of our knowledge, it is the only systematic computational investigation for ellipsoidal particles in a microchannel, but it was limited to oblate particles.

Prolate particles have been investigated even less than oblate particles. The only integrated experimental and computational study of prolate ellipsoids in a microchannel was performed by Masaeli *et al.*,<sup>13</sup> who used prolate particles of different aspect ratios and compared experimental results with lattice Boltzmann and finite element simulations. They experimentally and computationally studied the shape-based separation of prolate ellipsoid and applied the results to the enrichment of artificial beads and yeast. In that work, they distinguished between an in-plane rotation, when the particle rotates around the  $y$ -axis, and out-of-plane rotation, when there is any other component of rotation. Increasing the particle Reynolds number from 0.3 to 0.75, the percentage of in-plane rotations increases, and the rotational behavior is tumbling. They have also compared the period of rotation from their simulations to the theoretical value from Jeffery's theory, mainly observing no significant variation and concluding that inertia has no notable effect on it. However, inertia reduced the infinite number of Jeffery's orbits to just one stable orbit, implying that the starting orientation does not influence the final equilibrium orbit. They observed how the rotation of the particles is responsible for the shape-dependent separation. Higher aspect ratio prolates focus closer to the center of the channel since the repulsive wall lift from the wall is stronger, when the major axis of the particle is aligned perpendicular to the flow during the rotation. Finally, similar to what was reported by Hur *et al.*,<sup>21</sup> they confirmed that spherical and prolate particles with equivalent diameters have similar final equilibrium positions and that the maximum rotational diameter is the main parameter responsible for the focusing positions. Yet, since these studies focused on experiments and applications,<sup>13,21</sup> a limited range of confinement ratios were investigated computationally. More important, the transient migration dynamics was less explored than the final focusing positions in these studies.

In this work, we systematically explored the inertial migration dynamic behavior of prolate particles in a straight rectangular microchannel. We numerically investigated the effects of different shape aspect ratios and confinement ratios using smoothed particle hydrodynamics (SPH). Our computational study serves as the first systematic investigation of the inertial migration behavior of prolate particles in a microchannel. We not only studied how the focusing position and migration dynamics changes for prolate particles of different sizes and aspect ratios but also examined the rotational behavior, angular velocity, downstream focusing length, and migration trajectory, mapping their migration dynamics. For the cases with high confinement ratio, we observed a new logrolling motion of prolate ellipsoids in our simulations, for the first time. This new predicted result was confirmed by our microfluidic experiments on cell aggregates with similar shape aspect ratio and confinement ratio.

## II. METHODS

### A. SPH modeling approach

SPH is a mesh-free Lagrangian method, originally designed for astrophysical problems,<sup>24</sup> but it is also widely employed for various

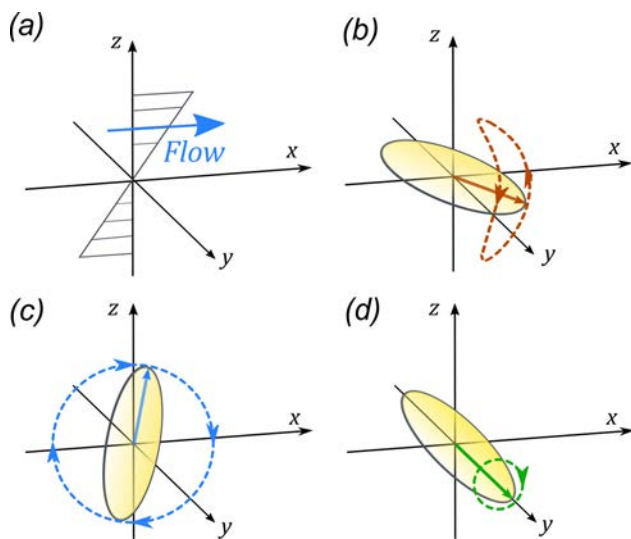


**FIG. 1.** (a) The gradient of velocity lies on the  $x$ - $z$  plane, with the fluid flowing in the  $x$  direction. The vorticity axis, perpendicular to the flow-gradient plane, corresponds to the  $y$  axis. (b) Kayaking motion of a prolate particle. (c) Tumbling motion when the particle is aligned with the  $z$  axis and tumbles around the vorticity axis, maintaining its vertical orientation, and the logrolling motion (d), when the particle is aligned with the vorticity axis.

fluid mechanics problems.<sup>25,26</sup> In the classical SPH approach, a state equation for a weakly compressible fluid is used to approximate incompressibility of the Navier–Stokes equations.<sup>27</sup> The general idea of SPH is to represent the fluid domain with Lagrangian particles, that is, SPH particles. Each of these particles has its own mass, velocity, energy, and other properties. Navier–Stokes equations are discretized using SPH particles, and a set of field variables, such as density and velocity, are interpolated by means of a kernel function, which decays to zero within a range of the smoothing length  $h$ . For each field variable  $f$ , the local average at position  $r_i$  is computed as

$$f(r_i) = \sum_j m_j \frac{f_j}{\rho_j} W(r_i - r_j), \quad (1)$$

where  $m_j$  and  $\rho_j$  are the value of mass and the density of the particle at position  $r_j$  and  $W$  is a kernel function that approximates the Dirac delta function. One possible kernel, proposed originally by Lucy, is a bell-shape kernel function.<sup>24</sup> Other popular kernel functions include the Gaussian, cubic spline, and B-spline, fourth and fifth spline.<sup>28</sup> Although SPH has been applied and validated for many fluid mechanics applications, it has not been widely used for inertial microfluidic simulations. We successfully applied SPH to study the transient motion of rigid spheres in straight rectangular channels<sup>29</sup> and the computational predictions match well with the high-speed fluorescence imaging trajectories, demonstrating that SPH is a reliable modeling approach in predicting the trajectory and equilibrium position of spherical particles in inertial microfluidics. The force and pressure on the particle  $i$  are given as

$$\mathbf{F}_i = - \sum_j m_i m_j \left( \frac{P_i}{\rho_i^2} + \frac{P_j}{\rho_j^2} \right) \nabla_j W_{ij} + \sum_j \frac{m_i m_j (\mu_i + \mu_j)}{\rho_i \rho_j} \left( \frac{1}{r_{ij}} \frac{\partial W_{ij}}{\partial r_i} \right), \quad (2)$$

$$P(\rho) = \frac{c_0^2 \rho_0}{7} \left[ \left( \frac{\rho}{\rho_0} \right)^7 - 1 \right]. \quad (3)$$

Equation (2) is the final momentum equation, where for two interacting particles  $i$  and  $j$ ,  $m$  is the mass,  $\rho$  is the density,  $P$  is the pressure tensor,  $W_{ij}$  is the kernel function,  $\mu$  is the dynamic viscosity, and  $r$  is the position vector of the considered particle.

The Tait equation of state [Eq. (3)] computes the pressure as a function of the local density and the temperature, where  $c_0$  is the speed of sounds and  $\rho_0$  is the density at zero applied stress. It is combined with Eq. (2), namely, Morris expression,<sup>30</sup> for laminar viscosity in our simulations.

## B. Simulation setup

In the current study, we applied a similar setup as in our previous work.<sup>29</sup> We used weakly compressible SPH with the Lucy kernel function, with a smoothing length of  $2 \mu\text{m}$ , and implemented it in LAMMPS.<sup>31</sup> The flow is generated by applying a constant body force to all particles, namely, the fluid and the rigid prolate particles, using periodic boundary conditions (PBCs). Although more sophisticated procedures could be implemented to generate a pressure-driven flow in the channel,<sup>32</sup> the ease of handling PBCs in SPH makes the body

force solution preferable to other techniques.<sup>33,34</sup> We computed the Reynolds number as  $Re = \frac{v_{\text{ave}} D_h \rho}{\mu}$ , where  $v_{\text{ave}}$  is the average velocity in the channel, and  $D_h$  is the hydraulic diameter computed as  $\frac{2WH}{W+H}$ , where  $W$  and  $H$  are the channel width and height, respectively. The density  $\rho$  and viscosity  $\mu$  of the SPH particles constituting the fluid were set to the water's value  $1000 \text{ kg/m}^3$  and  $10^{-3} \text{ Pa s}$ . The incompressibility of the flow is enforced by setting the speed of sound  $c_0$  at least ten times greater than the maximum velocity in the system.

The initial lattice of SPH particles was divided into groups, each one assigned with specific properties. The non-spherical prolate object to be simulated was created by defining an ellipsoidal region whose constituting SPH particle behaves as a single rigid body using LAMMPS *fix rigid* command. In addition, we took into account for the no-slip boundary conditions, modeling the interaction between fluid particles and the walls following the procedure described by Morris *et al.*<sup>30</sup> An artificial velocity was constructed for the particles at the boundaries, and it was used to compute the viscous forces.<sup>30</sup> The flow develops in the X direction, and it is confined by fixed particles constituting the channel walls. Finally, all the relevant information (position of the center of mass, angular velocity, torque, force, etc.) of the rigid prolate is recorded throughout the simulations. We tracked the entire migration of the particle by dumping the position of the SPH particles and visualizing it with VMD (visual molecular dynamics).<sup>35</sup>

## C. Device fabrication and high-speed imaging in experiments

A straight microfluidic channel was fabricated in polydimethylsiloxane (PDMS) using a dry film master. The process for making the dry film master is detailed in our previous work.<sup>36</sup> Briefly, a  $150 \times 50 \mu\text{m}^2$  rectangular straight microchannel was patterned on a 3 in. silicon wafer using dry film (ADEX 50, DJ MicroLaminates Inc., USA). The microchannel was then replicated in PDMS (Sylgard 184, Dow Corning®, USA), which was bonded to  $1 \times 3$  in. glass slides (Fisher Scientific, USA) to form sealed devices after  $\text{O}_2$  surface plasma treatment (PE-50, Plasma Etch Inc., USA) for 20 s. Inlet and outlet ports were made using a biopsy punch with an outer diameter of 1.5 mm (Ted Pella Inc., USA). Cell sample solution was loaded in a syringe (Norm-Ject®, Air-Tite Inc., USA), which was connected to 1/16 in. Tygon® tubing (Cole-Palmar, USA) using proper fittings (IDEX Health & Science LLC, USA). The other end of the tubing was secured to the device inlet. A syringe pump (Legato 200, KD Scientific Inc., USA) was used to sustain stable flow rate of  $300 \mu\text{L}/\text{min}$ . The microchannel was placed on the stage of an inverted microscope (IX83, Olympus America, USA). Images of cell aggregates inside the microchannel were acquired using a high-speed camera (Mini AX200, Photron USA, Inc.). The frame rate was 25 000 fps, and the exposure time was  $1 \mu\text{s}$ .

## D. Cell sample preparation

Non-small-cell lung cancer (NSCLC) cell line A549 was cultured in RPMI 1640 medium supplemented with 10% (v/v) fetal bovine serum (FBS), and 1% (v/v)  $100\times$  antibiotic–antimycotic solution in an incubator at  $37^\circ$  and 5%  $\text{CO}_2$ . Cell aggregates were formed in the low attachment plates, which were made by coating 12-well plate with anti-adherence solution (Stemcell Technology, Vancouver, Canada).<sup>37</sup> Anti-adherence solution coated the entire well bottom, and excess was

removed. Plates treated with anti-adherence solution were placed in a biosafety hood overnight under UV exposure until completely dry. Then, a 1 ml of A549 cell suspension was added into each well at 500 K cells/mL. After two days of culture, cell aggregates formed and were imaged. Cell aggregates were fixed using 4% paraformaldehyde (PFA) for 20 min and rinsed in phosphate buffered solution (PBS) before they were run into the microchannel.

### III. RESULTS AND DISCUSSION

#### A. Validation of SPH model

We first compared values of orbit period with Jeffery’s theory.<sup>17</sup> Jeffery’s theory shows that an ellipsoidal particle, in an unbounded linear shear flow, rotates along the so-called Jeffery orbits: a set of infinite orbits that depend on the initial particle orientation. The time required to complete one orbit, the period of rotation, is given as

$$T = \frac{2\pi}{\gamma} \cdot \left( \frac{1}{\lambda} + \lambda \right),$$

where it is inversely proportional to the shear rate  $\gamma$ , and it increases for higher values of the particle aspect ratio  $\lambda$ . We set up a simulation of a simple shear flow, generated by two parallel plates moving in opposite directions. The prolate particle was located halfway between the two plates, and the period of rotation was computed from the simulation. We set the distance of the plates to 80  $\mu\text{m}$  and their velocity to 10, 15, and 25 mm/s generating three different values of shear rate. Our results in Fig. 2 are in agreement with the theoretical values. Considering the lowest value of shear rate we used (250  $\text{s}^{-1}$ ), for a prolate with  $\lambda = 3$ , the theoretical value predicted by the formula is 0.0837 s, and the value from our simulation was  $T = 0.0842$  s. Similarly, for  $\lambda = 5$ , we got  $T = 0.1315$  s vs an expected value of 0.130 s.

We also validated our model against an existing numerical study for oblate particles that employs an immersed boundary method (IBM) in square and rectangular microchannels.<sup>23</sup> We investigated three different cases, to test our model in capturing the characteristic behaviors observed in the study. In Fig. 3, the cross-sectional view of the channels is shown. The dashed red line is the reference trajectory from Lashgari *et al.*<sup>23</sup> The circle and triangle indicate the initial and

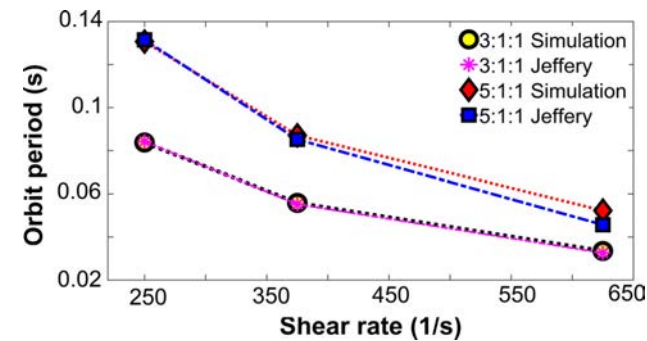


FIG. 2. Orbits period from Jeffery’s formula<sup>17</sup> (red diamonds) and the result from our SPH simulations in a simple shear flow (blue squares). Higher aspect ratios prolate particles rotate slower; namely, 5:1 prolates exhibit higher periods of rotation than the 3:1’s. In addition, for increasing values of shear rate, the rotational period decreases for all the ellipsoids.

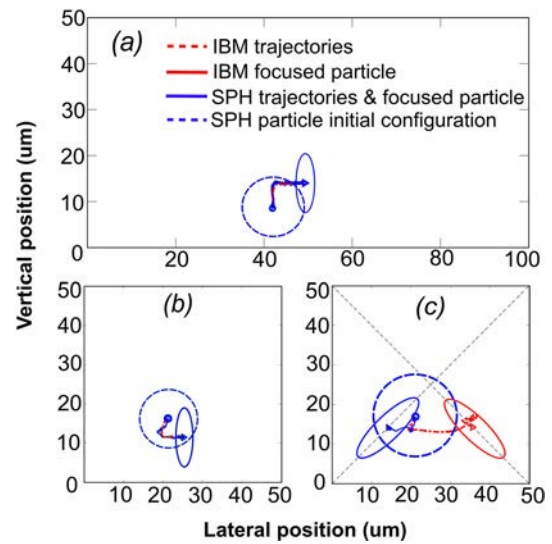


FIG. 3. Inertial migration of oblate particles in the cross-sections in square and rectangular channels reproduced from Lashgari *et al.*<sup>23</sup> investigation. (a) Oblate particle in a rectangular channel, with a starting position of 42 and 8.6  $\mu\text{m}$  in  $y$  (horizontal) and  $z$  (vertical), respectively. (b) Oblate in a square channel, with the same diameter of the oblate ellipsoid in the rectangular channel, but starting in position 20 and 17  $\mu\text{m}$ . (c) Oblate particle with a radius of 10.3  $\mu\text{m}$  starting at 20 and 17  $\mu\text{m}$ .

final position of the center of mass of the oblate spheroid. We set the initial and final oblate configuration to be the same of the reference paper by Lashgari *et al.*<sup>23</sup> and reported them with a blue dashed and solid line, respectively. We first simulated the motion of an oblate spheroid in a square channel of side  $H$ , with a cross-section of  $50 \times 50 \mu\text{m}^2$  as shown in Fig. 3(b). We set the body force to match the bulk  $\text{Re} = 100$  used in the study. We tested the first oblate matching the relation  $\frac{H}{D_0} = 3.466$ , corresponding to a diameter  $D_0$  of 14.4  $\mu\text{m}$  related to our channel dimensions. For this case, Lashgari *et al.*<sup>23</sup> monitored the orientation of the oblate using a unit vector  $\mathbf{n}$  parallel to the symmetry axis of the particle and then tested different starting positions. We selected one of them, and we imposed the same starting orientation, namely,  $\mathbf{n} = [0, 1, 0]$ . We obtained the same final focusing position and orientation with SPH. The transitional behavior is a chaotic motion shifting to tumbling, rapidly turning into a logrolling motion, namely, with  $\mathbf{n} = [1, 0, 0]$ . The focusing position was 25 and 12  $\mu\text{m}$  away from the wall in the lateral and vertical positions, respectively. Lashgari *et al.*<sup>23</sup> reported that the particle focused on a vertical distance of 0.26H from the center, corresponding to 12  $\mu\text{m}$  away from the wall for  $H = 50 \mu\text{m}$ , thus matching our predicted position.

A good match was also obtained in the second case for an oblate particle with a size of 20.6  $\mu\text{m}$ . In this case, Lashgari *et al.*<sup>23</sup> reported a focusing behavior, which was inclined-rolling on the diagonal of the microchannel. The final focusing position was 14.5  $\mu\text{m}$  in both directions. The focusing dynamics and position match the results also in this case. However, we noted that the oblate migrates toward to nearest diagonal from which it was released, as shown in Fig. 3(c). On the contrary, Lashgari *et al.*<sup>23</sup> reported that the larger oblate migrated to the

opposite diagonal. In our case, the first part of the trajectory is the same as the reference, but then the particle migrates toward the closest diagonal from where it is released. Only for this case, in Fig. 3(c), we included a solid red line for the oblate spheroid focused at the opposite diagonal of the channel (reference IBM results from Lashgari *et al.*). The peculiar behavior was explained by the authors in terms of the streamwise rotation, that in the case of the larger oblate does not decay to zero, as it does for the smaller particles. The streamwise rotation would cause an initial acceleration of the oblate toward to center of the channel, and eventually, it will reach the opposite diagonal. We plotted the streamwise angular velocity from our simulations, and we did not observe this behavior. The discrepancy might be due to the different ways in which the solid and fluid phase interaction is handled by the different numerical methods adopted (SPH and IBM).<sup>38</sup> We observed that the rotation rate increases first and then decreases, following the same trend found in all the other cases.

Finally, since our investigation of prolate particles is in rectangular cross-section, we also tested a case of oblate particles in a rectangular duct of aspect ratio 2 against the result by Lashgari *et al.*<sup>23</sup> as shown Fig. 3(a). For this, we kept one side at  $H = 50 \mu\text{m}$  and then scaled the top and bottom walls to  $100 \mu\text{m}$ . In addition, the constant body force was chosen so that the resulting bulk Reynolds number was close to 100. We also changed the box length to  $200 \mu\text{m}$ , twice the length used for the square channel. Lashgari *et al.*<sup>23</sup> reported that the distance between the centers of the oblate and the channel is 0.22H,

corresponding to a distance  $11 \mu\text{m}$  from the center and  $14 \mu\text{m}$  from the wall. This matches our results, where the oblate focuses in a vertical position oscillating between  $13.8$  and  $14.2 \mu\text{m}$  from the bottom wall. We also confirmed the logrolling behavior for this case. In Fig. 3, the dashed-red line represents the trajectories shown in the paper and are here plotted against our results from SPH simulations. Overall, the initial configuration was set the same as the reference cases for all three simulations. The final focusing behavior and position were confirmed for all cases, except for the bigger oblate, where the focusing position is on the closest diagonal from which it is released.

**B. Inertial migration of prolate particles in a rectangular microchannel**

After the validation of our SPH model, we focused on the transient migration behavior of prolate particles in a straight channel with a rectangular  $50 \times 25 \mu\text{m}^2$  cross-section. The length of the simulation box was set as twice the width of the channel, thus  $100 \mu\text{m}$ , and  $Re = 50$  for all cases. We found that different values of confinement ratio and particle aspect ratio affect the migration dynamics of prolate particles in terms of focusing length and time, period of rotation, angular velocity, and rotational motion. These values are reported in Table I and discussed throughout Subsections III C–III F.

We defined the confinement ratio  $K$  for each particle as the largest dimension of the prolate, representing its rotational diameter, divided by the smallest side of the channel ( $25 \mu\text{m}$  in our cases). For

**TABLE I.** For the two groups of particle aspect ratios, the table contains all the 18 cases that were investigated in the present study (nine cases for the 3:1:1 prolate spheroids and nine cases for the 2:1:1). These simulations are further organized into subgroups of three cases each, corresponding to the different confinement ratios  $K$ . For each value of  $K$ , the three starting positions are listed. Overall, the table is comprehensive of the dimensions  $a$  and  $b$  (major and minor axis) for each prolate ellipsoid, together with the final focusing position, the maximum values of the angular velocity about the  $y$  axis  $\omega_{\text{max}}$ , the focusing time  $t_f$  and the focusing length  $L_f$ . Each particle is released with its longest dimension aligned with the  $x$  axis, which is the direction of the flow.

Aspect ratio	$a$ ( $\mu\text{m}$ )	$b$ ( $\mu\text{m}$ )	$K$	Starting position ( $\mu\text{m}$ )	Rotational mode	Focusing position ( $\mu\text{m}$ )	$\omega_{\text{max}}$ (kHz)	$t_f$ (ms)	$L_f$ (mm)
3:1:1	9.0	3.0	0.36	(10,10)	Tumbling	(25,6.8)	42.9	8.5	25.5
				(15,5)		(25,6.8)	44.5	10	33
				(25,10)		(25,6.3)	44.5	7	23.1
	13.8	4.6	0.55	(10,10)	Tumbling	(25,7.8)	34.2	3.8	13.3
				(15,5)		(25,7.7)	35.8	3	10.2
				(25,10)		(25,7.7)	35.0	3	10.8
	19.2	6.4	0.77	(10,10)	Logrolling	(25,7.2)	22.6	3.8	12.1
				(15,5)		(25,7.2)	23.1	3	9.6
				(25,10)		(25,8)	26.7	6	19.8
2:1:1	6.88	3.44	0.27	(10,10)	Tumbling	(25,6.1)	42.9	9	27.9
				(15,5)		(25,6.1)	42.1	9	29.7
				(25,10)		(25,6.3)	41.4	7	23.1
	10.52	5.26	0.42	(10,10)	Tumbling	(25,7.4)	35.0	6	20.4
				(15,5)		(25,7.2)	35.0	6	19.8
				(25,10)		(25,7.2)	35.8	6	19.8
	14.6	7.3	0.58	(10,10)	Tumbling	(25,7.8)	31.8	2.2	7.15
				(15,5)		(25,7.8)	31.8	2	6.6
				(25,10)		(25,8)	31.8	2	6.6
1.5:1:1	18.50	12.50	0.74	(15,5)	Logrolling	(25,7.9)	17.5	2.1	6.3
4:1:1	19	4.75	0.76	(15,5)	Logrolling	(25,7.4)	24.2	3	9
5:1:1	19	3.8	0.76	(15,5)	Logrolling	(25,7.2)	24.9	4.1	12.3

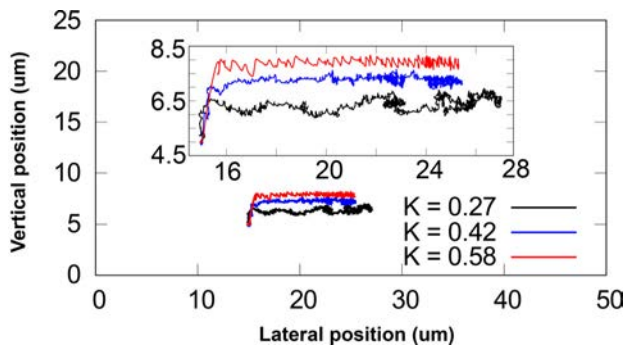


**FIG. 4.** Cross-sectional view of the trajectories for the 2:1:1 prolate spheroids with different values of confinement ratios. The plot shows the particles starting from the same initial position, and it can be noticed that the vertical focusing position is progressively more distant from the bottom wall as the particle size is increased. The particle with the lowest confinement ratio goes beyond the lateral centerline and then goes back focusing on the lateral centerline.

each value of confinement ratio, we explored three different starting positions and used them for all cases. We located the center of mass of the particle at (10,10), (15,5), and (25,10) initially, thus progressively closer to the center of the channel. We refer to them as starting positions 1, 2, and 3. First, we studied the different sizes for the same aspect ratio, and then, we made a cross-comparison among different aspect ratios. The starting orientation for all the particles is with their rotational diameter aligned with the flow direction.

In general, the trajectories present small oscillations of the center of mass of the particle, due to the rotation of the particles. Moreover, the vertical focusing position increases with the size of the particles. For example, for the aspect ratio 3:1:1, the particles focus at 6.8, 7.6, and 8 μm when increasing the confinement ratio. Similarly, we observed a final vertical position of 6.2, 7.4, and 8 μm for the prolate particles with an aspect ratio of 2:1:1. The migration of the center of mass of the latter is reported in Fig. 4, where a zoom on the trajectories is included within the cross-section. For the case of the smallest confinement ratio, the trajectory experiences an overshoot in the lateral position, going beyond the channel mid-line and then going back toward the center, due to inertia. This behavior has been already reported in the literature.<sup>39</sup>

### C. Effect of the confinement ratio and particle aspect ratio on the rotational dynamics

We investigated prolate particles of aspect ratios 2:1:1 and 3:1:1, meaning that the longest dimension of the particle is, respectively, 2 and 3 times longer than the other dimensions.

The rotational behavior, which is mostly observed, throughout all the cases we have investigated, is a transition from a chaotic behavior, namely, a combination of the three main motions shown in Fig. 1, to kayaking and eventually tumbling. This trend is consistently observed for all starting positions for all cases, except for the starting positions 1 and 2 for the value of  $K = 0.768$  in the 3:1:1 case. For these two cases, the final rotational behavior is logrolling, while the particle starting from position 3 ends up kayaking. As a consequence, the vertical focusing position is 7.2 μm, thus closer to the wall with respect to the

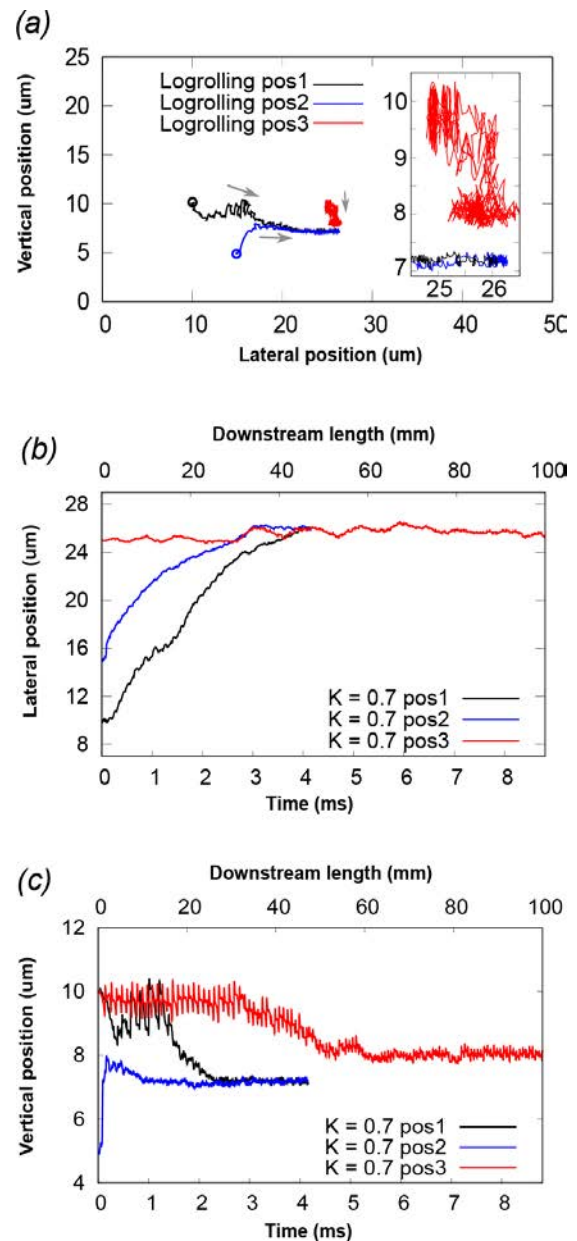


**FIG. 5.** (a) Cross-sectional view of the trajectories for the 3:1:1 prolate spheroids with a value of  $K = 0.77$ . The prolate ellipsoids starting in positions 1 and 2 reach the same stable equilibrium position around the lateral centerline, with a final logrolling behavior. The particle released at the center stabilizes into a kayaking motion; thus, its vertical equilibrium position is higher than other two cases. (b) Variation of the lateral position of the center of mass vs time and downstream length. (c) Variation of the vertical position of the center of mass vs time and downstream length.

same particle starting in position 3, which focuses at 8 μm, as shown in Fig. 5. The reason is that, when it is kayaking, the particle is subjected to a greater lift that pushes it away from the wall, like what is reported with the numerical observations by Masaeli *et al.*<sup>13</sup> for tumbling particles. In the cases where the particle logrolls, the repulsive lift

is much smaller; therefore, the particle gets slightly closer to the nearest wall. Overall, these cases show that the same particle undergoes two different rotational behaviors, depending on its size and its initial position within the channel cross-section. In Fig. 5, we have also plotted how the lateral and vertical positions of the center of mass changes over time and also with respect to the downstream length. These figures provide a sense of the speed of the migration of the particle. First, it rapidly moves toward the equilibrium manifold, represented in a fast variation of the vertical position, followed by a slow migration toward the channel centerline, according to the model presented by Zhou and Papautsky for spherical particles.<sup>40</sup>

The equilibrium manifold is an equilibrium region where the particle is equilibrated in the vertical direction, and it experiences a lateral migration toward the equilibrium position. It was described also from Lashgari *et al.* and other previous works.<sup>41,42</sup>

The logrolling behavior has not been reported in the literature, where the studies converge on the fact that prolate particles always tumble in a Poiseuille flow at moderate Reynolds numbers, similar to the behavior in shear flows. We found that the parameter mainly responsible for the logrolling mode is not the aspect ratio, but the confinement ratio. Indeed, the biggest particles we simulated for both aspect ratios 2:1:1 and 3:1:1, using the same volume, had a different rotational diameter: 14.6 and 19.2  $\mu\text{m}$ , respectively. We performed additional simulations where we fixed aspect ratio but inverted values of the confinement ratio. As expected, the 3:1:1 particle that in the original case was logrolling is now tumbling, and the 2:1:1 particle that was tumbling originally is now logrolling. This behavior is due to increase in the rotational diameter. We identified the threshold value of confinement ratio for the logrolling to occur, assuming that the particle is sufficiently distant from the center, so it can develop all the transitional behaviors described before. First, since prolate spheroids with  $d_{\text{rot}} = 14.6 \mu\text{m}$  tumble and those with  $d_{\text{rot}} = 19.2 \mu\text{m}$  logroll, we ran five additional cases with 3:1:1 particles whose rotational diameter was 15.6, 16.6, 17.6, 18, and 18.6  $\mu\text{m}$  corresponding to confinement ratios of 0.624, 0.664, 0.704, 0.720, and 0.744, respectively. We observed that for the first three cases, the final tumbling motion was confirmed. Confinement ratio  $K = 0.720$  leads to a final kayaking motion and represents an approximate threshold value for a change in the final rotational behavior. Above this value, the particle will logroll.

In addition to the particle aspect ratios 2:1 and 3:1, we have also tested prolate particles with lower aspect ratios 1.1:1, 1.2:1, and 1.5:1 and higher aspect ratios 3.2:1, 3.5:1, 4:1, and 5:1. We set the confinement ratios of these particles above the approximate threshold obtained for the aspect ratios 2:1 and 3:1. The starting position for all these cases is (15,5). We did not test whether the threshold value was exactly the same also for these additional cases, but we confirmed that the general trend is respected, namely, that values of confinement ratios above the estimated threshold of  $K = 0.72$  yield a final logrolling behavior. Some of these cases are included in Table I.

The logrolling motion of a prolate particle was also confirmed in our experiments in a straight rectangular channel with a cross-section of  $150 \times 50 \mu\text{m}^2$ . The flow rate was set to 300  $\mu\text{L}/\text{min}$ , corresponding to  $\text{Re} = 50$ , and the particle was an aggregate of fixed cells, behaving like a rigid body. The aggregate was not perfectly symmetrical, but very close to an axisymmetric 3:1:1 prolate, with a rotational diameter of 50  $\mu\text{m}$  ( $K = 1$ ). We simulated the same experimental conditions and the

predicted logrolling motion agrees well with the experimental observation. The comparison between the imaging top view of the channel and the results of our simulation is shown in Fig. 6 (Multimedia view).

#### D. Effect of the initial position and orientation on the rotational behavior

The effect of the particle's initial location and alignment on its migration and focusing behaviors is still not clear for both shear flows and Poiseuille flows. It has been shown that oblate spheroids logroll, regardless of their initial conditions, but in the current literature, there is no such information for prolate particles. Considering the group of prolate spheroids with  $K = 0.768$  [Fig. 5(a)], the particle starting in position 3 begins with a tumbling mode and stabilizes in a kayaking motion. On the other hand, we observed that the particles starting in positions 1 and 2 exhibit a chaotic rotational behavior initially, but begin kayaking and rolling at the same time while migrating laterally.

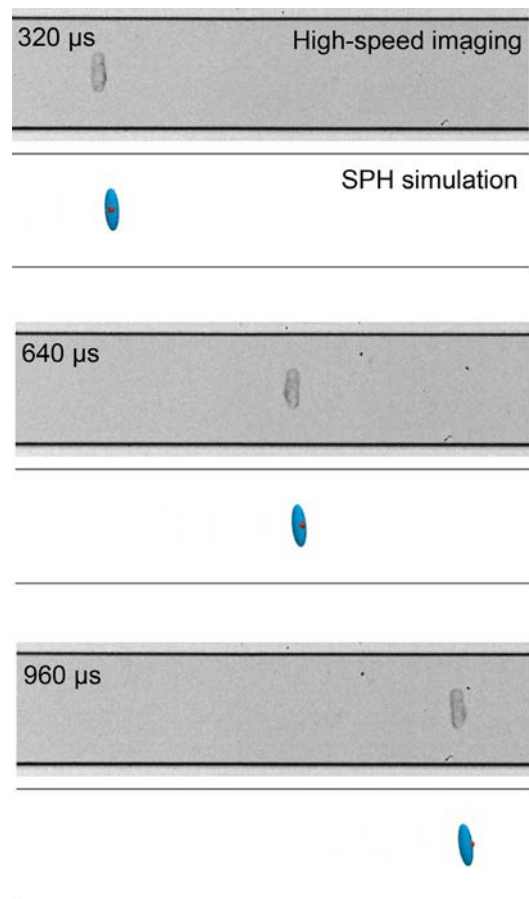


**FIG. 6.** Top view of a logrolling prolate particle at three different time intervals. The frames from the videos of the simulation and experimental observation have been juxtaposed. The cell aggregate logrolls while moving downstream, and its center of mass is located approximately at the channel center. The same behavior is observed from the computational results. A red marker was placed on the surface of the modeled prolate particle to help visualize its motion. Multimedia view: <https://doi.org/10.1063/5.0100963.1>

The dominant orbit progressively flattens, while the particle approaches the lateral centerline and the kayaking motion completely transitions into logrolling configuration. The change in the rotational behaviors when changing the starting position might be also due to the initial orientation of the particle and its location within the parabolic velocity profile in the channel. If the particle is released sufficiently far away from the channel center, where the velocity of the fluid is lower, it will experience a progressively increasing velocity of the fluid while migrating laterally toward the center, and its transitional behavior will follow the one described before. If the particle is released close to the center, like the starting position 3, its initial configuration will determine the final rotational behavior. At the center, where the fluid velocity is higher, the particle lateral migration is minimal, and it cannot go through the different rotational modes leading to the logrolling. To confirm, we set up an additional simulation in which we released the particle at the starting position 3, but with its rotational diameter perpendicular to the flow direction, namely, already in a logrolling setup. The particle migrates downward, reaching a vertical focusing position of  $7.2 \mu\text{m}$ , and exhibits the final logrolling behavior.

### E. Effect of particle aspect ratio and confinement ratio on the period of rotation

We also investigated the period of rotation, whose dependency on the size and aspect ratio was still not fully clarified in the previous studies. Hur *et al.*<sup>21</sup> concluded that the orbit period does not depend on the aspect ratio, but on the confinement ratio. On the other hand, Masaeli *et al.*<sup>13</sup> reported that the period of rotation increases along with the aspect ratio, following Jeffery's formula.<sup>17</sup> Computation of this parameter from our simulations reveals that both can be true depending on the particle's aspect ratio and confinement ratio. We observed a higher period of rotation for higher aspect ratio particles and also for increasing values of confinement ratio, with a fixed aspect ratio. However, the magnitude of this difference is greater for distinct aspect ratios and the size contributes to minor changes. Moreover, a particle that is logrolling rotates about three times faster than a particle with the same volume that is tumbling.

### F. Effect of particle aspect ratio and confinement ratio on the angular velocity

Our results show that the angular velocity with respect to the vorticity axis is not constant, but is periodic, with minimum values when the particle is aligned with the flow direction and maximum values when the particle is perpendicular to the top and bottom walls. This characteristic was already reported in several studies.<sup>17,43</sup> In Fig. 7, we show the differences in the angular velocities of particles with a different aspect ratio, but with the same confinement ratio. The number of peaks gives additional information on the number of rotations in the same amount of time, illustrating how the orbit period differs. Figure 7(a) shows two particles undergoing a tumbling motion, while Fig. 7(b) shows particles with a higher confinement ratio that stabilize in a logrolling motion. We found that within the same aspect ratio, smaller particles show higher peaks for the maximum angular velocity. The minimum values, when the particle is aligned with the flow direction, change with the aspect ratio. The group of 2:1:1 prolate particles, shown in Fig. 8, exhibits a minimum angular velocity close to 2 kHz,

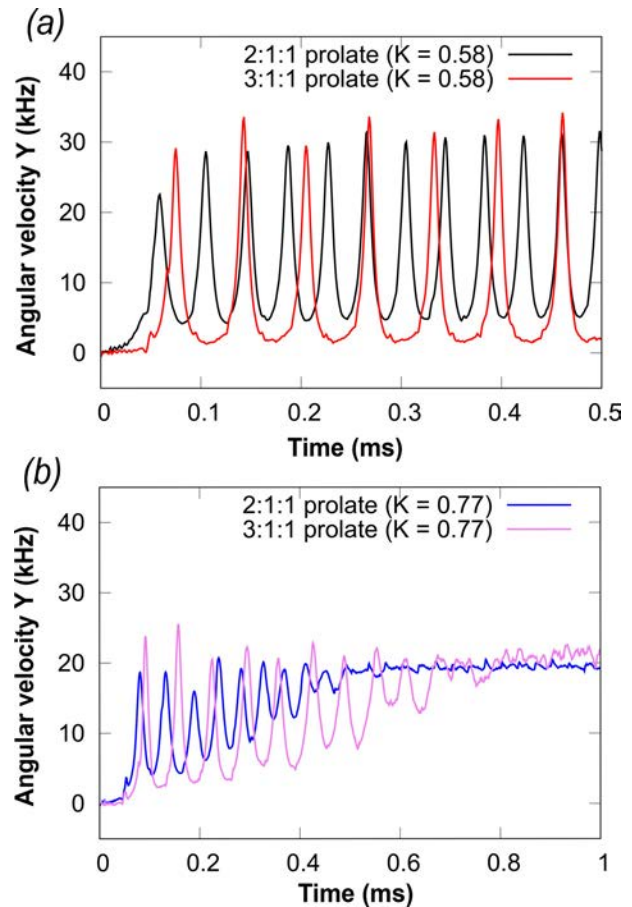


**FIG. 7.** Angular velocity around the y axis (vorticity axis). (a) The trend shows the periodicity of the angular velocity and the different magnitude for two tumbling particles with the same confinement ratio and different aspect ratios. It can be also noticed how the frequency of rotation is greater for the lower aspect ratio prolate spheroid. (b) When the rotational diameter is increased, the particles end up logrolling and the angular velocity becomes almost constant, but with slightly different values according to the aspect ratio.

whereas it is on the order of 6 kHz for the 3:1:1 group. The minimum and maximum values of the angular velocity of a logrolling particle are very close, because the oscillations are small and the magnitude almost constant, unlike tumbling particles where the periodicity is non-negligible.

## IV. POTENTIAL APPLICATIONS

The research areas that can benefit from this study include, but not limited to, the medical and biological fields, food, and environmental technologies.<sup>44–47</sup> Among the studies that use shape as a biomarker to perform separation and sorting, Li *et al.* successfully developed a device for shape-based separation of a microalga for biomass production, whose shape is a useful indicator for its cell cycle status, environmental condition, and many more.<sup>48</sup> It demonstrates how cells with a different aspect ratio focus on different lateral positions and can passively separate with a throughput of 1300 cells/s. Similarly, Liu *et al.* performed a shape-based separation with *Cerevisiae* cells,

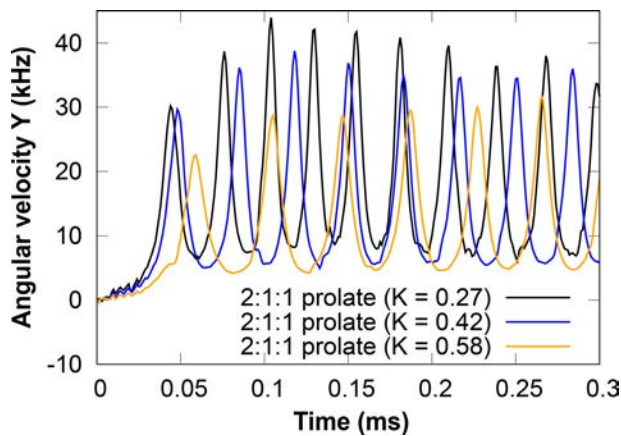


**FIG. 8.** The confinement ratio affects the angular velocity of tumbling particles with the same aspect ratio. The maximum value reached during the rotation is higher for smaller particles, which are also characterized by a higher frequency of rotation. Only a part of the simulation is plotted, but the same trend also extends for the rest of the simulation.

showing that a variation in shape leads to the migration to different lateral positions and with different velocities.<sup>49</sup> Feng *et al.* used a spiral microchannel to enrich and separate chromosomes from cell debris.<sup>50</sup> Their results show the possibility of separating chromosomes by exploiting their size and aspect ratio: the two factors influencing the final focusing position, thus elution location, in a spiral microchannel. Yuan *et al.* demonstrated for the first time the separation of cyanobacteria using viscoelastic microfluidics, exploiting the effects of different shapes.<sup>49</sup> The emerging studies using this technique suggest the benefit of inertial microfluidics to this kind of application, where particle shape and alignment are relevant. Numerical simulations can provide valuable information on the inertial migration of particles with various shapes by thoroughly exploring and tuning each parameter. Moreover, once the numerical method is validated, it can be used to predict and guide the experimental design. In addition, the simulations provide information that is not accessible experimentally, such as detailed flow and stress fields.

As reported by Behdani *et al.*, shape-based separation is a powerful tool, but the main limiting factors are the lack of a general framework to study the shape effects and the absence of a systematic work in the literature to address the multiple variables that can affect the migration dynamic.<sup>51</sup>

## V. CONCLUSIONS

We applied SPH modeling approach to investigate the effects of particle size and shape on its inertial behavior in a straight rectangular duct. We explored the behavior of prolate spheroids at  $Re = 50$ , testing a range of confinement ratios and two values of particle aspect ratios, and examined the migration dynamics within the channel. The general trend is that prolate ellipsoid migrates toward the channel lateral centerline and they assume a final tumbling rotational mode while moving downstream. However, when increasing the particle rotational diameter, thus its blockage ratio, the final rotational behavior can be either kayaking or logrolling, depending on the particle's initial position and orientation. This is the first time this logrolling behavior is

reported for prolate spheroids. The same particle can undergo a set of transitional behaviors and eventually logrolls if it is sufficiently distant from the center of the channel. If the particle is released near the center, where the fluid velocity is higher, the initial alignment will determine the final mode of rotation. We identified  $K = 0.72$  as an estimated threshold value above which the particle will logroll regardless of its aspect ratio.

In addition, we reported that the orbit period of tumbling particles depends on both the particle's rotational diameter and aspect ratio. Moreover, a prolate spheroid in a tumbling configuration exhibits a period angular velocity, which shows maximum peaks, when the particle is vertically aligned.

A prolate particle that is logrolling has an angular velocity that is almost constant, with a value close to the average velocity of a tumbling particle. The result and information provided will be valuable for all the applications of high-throughput separation, sorting, and analysis where particle shape and alignment are relevant. By choosing the proper channel cross-section and particle size and aspect ratio, the final focusing behavior can be controlled to obtain the logrolling behavior we reported in this study. This might be useful to allow the optical reading since the particle rotational axis is not changing over time. Also, a prolate ellipsoid could provide more surface area with respect to a spherical droplet or particle. In future work, higher values of the Reynolds number can be investigated to shed more light on the rotational behaviors in this condition, which are still not clear. This approach can be extended to different channel cross-sections and particle shapes to provide some design basis for shape-based separation and interrogation platforms and help their integration into Lab-on-Chip devices.

## ACKNOWLEDGMENTS

We would like to acknowledge partial support from the National Science Foundation and the industrial members of the Center for Advanced Design and Manufacturing of Integrated Microfluidics (NSF I/UCRC Award No. IIP-1841473).

G.L. and Z.P. are partially supported by NSF/DMS No. 1951526. Simulations were conducted on the supercomputer Theta in Argonne Leadership Computing Facility (ALCF) in the Argonne National Lab under Director's Discretionary (DD) allocation Modeling Corona Virus. This research used the resources of the Argonne Leadership Computing Facility, which is a DOE Office of Science User Facility supported under Contract No. DE-AC02-06CH11357. G.L. acknowledges Professor Guido Raos for supporting the discussion of the work.

## AUTHOR DECLARATIONS

### Conflict of Interest

The authors have no conflicts to disclose.

### Author Contributions

**Giuseppe Lauricella:** Data curation (lead); Formal analysis (lead); Investigation (lead); Methodology (lead); Validation (lead); Visualization (lead); Writing – original draft (lead); Writing – review and editing (lead). **Jian Zhou:** Data curation (supporting); Methodology (supporting); Writing – review and editing (supporting). **Qiyue Luan:** Data curation (supporting). **Ian Papautsky:**

Conceptualization (equal); Funding acquisition (supporting); Investigation (supporting); Writing – review and editing (equal). **Zhangli Peng:** Conceptualization (lead); Funding acquisition (lead); Investigation (lead); Writing – original draft (lead); Writing – review and editing (lead).

## DATA AVAILABILITY

The data that support the findings of this study are available within this article.

## REFERENCES

- 1<sup>J.</sup> Zhang, S. Yan, D. Yuan, G. Alici, N.-T. Nguyen, M. E. Warkiani, and W. Li, “Fundamentals and applications of inertial microfluidics: A review,” *Lab Chip* **16**, 10–34 (2016).
- 2<sup>S.</sup> Kalyan, C. Torabi, H. Khoo, H. W. Sung, S.-E. Choi, W. Wang, B. Treutler, D. Kim, and S. C. Hur, “Inertial microfluidics enabling clinical research,” *Micromachines* **12**, 257 (2021).
- 3<sup>X.</sup> Xu, X. Huang, J. Sun, R. Wang, J. Yao, W. Han, M. Wei, J. Chen, J. Guo, L. Sun *et al.*, “Recent progress of inertial microfluidic-based cell separation,” *Analyst* **146**, 7070 (2021).
- 4<sup>F.</sup> Alnaimat, S. Dagher, B. Mathew, A. Hilal-Alnqbi, and S. Khashan, “Microfluidics based magnetophoresis: A review,” *Chem. Rec.* **18**, 1596–1612 (2018).
- 5<sup>M.</sup> Bakir, “Electromagnetic-based microfluidic sensor applications,” *J. Electrochem. Soc.* **164**, B488 (2017).
- 6<sup>P.-H.</sup> Lu, Y.-D. Ma, C.-Y. Fu, and G.-B. Lee, “A structure-free digital microfluidic platform for detection of influenza A virus by using magnetic beads and electromagnetic forces,” *Lab Chip* **20**, 789–797 (2020).
- 7<sup>P.</sup> Zhang, H. Bachman, A. Ozcelik, and T. J. Huang, “Acoustic microfluidics,” *Annu. Rev. Anal. Chem.* **13**, 17 (2020).
- 8<sup>U.</sup> Kim, B. Oh, J. Ahn, S. Lee, and Y. Cho, “Inertia-acoustophoresis hybrid microfluidic device for rapid and efficient cell separation,” *Sensors* **22**, 4709 (2022).
- 9<sup>W.</sup> Chen, F. Shao, and Y. Xianyu, “Microfluidics-implemented biochemical assays: From the perspective of readout,” *Small* **16**, 1903388 (2020).
- 10<sup>W.</sup> Li, X. Tang, and L. Wang, “Photopyroelectric microfluidics,” *Sci. Adv.* **6**, eabc1693 (2020).
- 11<sup>J.</sup> M. Martel and M. Toner, “Inertial focusing in microfluidics,” *Annu. Rev. Biomed. Eng.* **16**, 371–396 (2014).
- 12<sup>J.</sup> Zhou, P. Mukherjee, H. Gao, Q. Luan, and I. Papautsky, “Label-free microfluidic sorting of microparticles,” *APL Bioeng.* **3**, 041504 (2019).
- 13<sup>M.</sup> Masaeli, E. Sollier, H. Amini, W. Mao, K. Camacho, N. Doshi, S. Mitragotri, A. Alexeev, and D. Di Carlo, “Continuous inertial focusing and separation of particles by shape,” *Phys. Rev. X* **2**, 031017 (2012).
- 14<sup>H.</sup> Amini, W. Lee, and D. D. Carlo, “Inertial microfluidic physics,” *Lab Chip* **14**, 2739–2761 (2014).
- 15<sup>J.</sup> Matas, J. Morris, and E. Guazzelli, “Lateral forces on a sphere,” *Oil Gas Sci. Technol.* **59**, 59–70 (2004).
- 16<sup>J.</sup> Cruz, T. Graells, M. Walldén, and K. Hjort, “Inertial focusing with sub-micron resolution for separation of bacteria,” *Lab Chip* **19**, 1257–1266 (2019).
- 17<sup>G.</sup> B. Jeffery, “The motion of ellipsoidal particles immersed in a viscous fluid,” *Proc. R. Soc. London, Ser. A* **102**, 161–179 (1922).
- 18<sup>T.</sup> Tohme, P. Magaud, and L. Baldas, “Transport of non-spherical particles in square microchannel flows: A review,” *Micromachines* **12**, 277 (2021).
- 19<sup>Y.</sup> Huang, R. L. Marson, and R. G. Larson, “Inertial migration of neutrally buoyant prolate and oblate spheroids in plane Poiseuille flow using dissipative particle dynamics simulations,” *Comput. Mater. Sci.* **162**, 178–185 (2019).
- 20<sup>T.-W.</sup> Pan, C.-C. Chang, and R. Glowinski, “On the motion of a neutrally buoyant ellipsoid in a three-dimensional Poiseuille flow,” *Comput. Methods Appl. Mech. Eng.* **197**, 2198–2209 (2008).
- 21<sup>S.</sup> C. Hur, S.-E. Choi, S. Kwon, and D. D. Carlo, “Inertial focusing of non-spherical microparticles,” *Appl. Phys. Lett.* **99**, 044101 (2011).
- 22<sup>S.</sup> R. Bazaz, A. Mashhadian, A. Ehsani, S. C. Saha, T. Krüger, and M. E. Warkiani, “Computational inertial microfluidics: A review,” *Lab Chip* **20**, 1023–1048 (2020).
- 23<sup>I.</sup> Lashgari, M. N. Ardekani, I. Banerjee, A. Russom, and L. Brandt, “Inertial migration of spherical and oblate particles in straight ducts,” *J. Fluid Mech.* **819**, 540–561 (2017).
- 24<sup>L.</sup> B. Lucy, “A numerical approach to the testing of the fission hypothesis,” *Astron. J.* **82**, 1013–1024 (1977).
- 25<sup>G.</sup> R. Liu and M. B. Liu, *Smoothed Particle Hydrodynamics* (World Scientific, 2003).
- 26<sup>P.</sup> Jonsson, P. Jonsén, P. Andreasson, T. S. Lundström, and J. G. I. Hellström, “Smoothed particle hydrodynamic modelling of hydraulic jumps: Bulk parameters and free surface fluctuations,” *Engineering* **8**, 386–402 (2016).
- 27<sup>R.</sup> A. Gingold and J. J. Monaghan, “Smoothed particle hydrodynamics: Theory and application to non-spherical stars,” *Mon. Not. R. Astron. Soc.* **181**, 375–389 (1977).
- 28<sup>S.</sup> M. Hosseini and J. J. Feng, “Pressure boundary conditions for computing incompressible flows with SPH,” *J. Comput. Phys.* **230**, 7473–7487 (2011).
- 29<sup>J.</sup> Zhou, Z. Peng, and I. Papautsky, “Mapping inertial migration in the cross section of a microfluidic channel with high-speed imaging,” *Microsyst. Nanoeng.* **6**, 105 (2020).
- 30<sup>J.</sup> P. Morris, P. J. Fox, and Y. Zhu, “Modeling low Reynolds number incompressible flows using SPH,” *J. Comput. Phys.* **136**, 214–226 (1997).
- 31<sup>S.</sup> Plimpton, “Fast parallel algorithms for short-range molecular dynamics,” *J. Comput. Phys.* **117**, 1–19 (1995).
- 32<sup>K.</sup> Lykov, X. Li, H. Lei, I. V. Pivkin, and G. E. Karniadakis, “Inflow/outflow boundary conditions for particle-based blood flow simulations: Application to arterial bifurcations and trees,” *PLoS Comput. Biol.* **11**, e1004410 (2015).
- 33<sup>T.</sup> Wu and J. J. Feng, “Simulation of malaria-infected red blood cells in microfluidic channels: Passage and blockage,” *Biomicrofluidics* **7**(4), 044115 (2013).
- 34<sup>A.</sup> Yazdani, M. Deng, B. Caswell, and G. E. Karniadakis, “Flow in complex domains simulated by dissipative particle dynamics driven by geometry-specific body-forces,” *J. Comput. Phys.* **305**, 906–920 (2016).
- 35<sup>W.</sup> Humphrey, A. Dalke, and K. Schulten, “VMD: Visual molecular dynamics,” *J. Mol. Graph.* **14**, 33 (1996).
- 36<sup>P.</sup> Mukherjee, F. Nebuloni, H. Gao, J. Zhou, and I. Papautsky, “Rapid prototyping of soft lithography masters for microfluidic devices using dry film photoreist in a non-cleanroom setting,” *Micromachines* **10**, 192 (2019).
- 37<sup>Q.</sup> Luan, J. H. Becker, C. Macaraniang, M. G. Massad, J. Zhou, T. Shimamura, and I. Papautsky, “Non-small cell lung carcinoma spheroid models in agarose microwells for drug response studies,” *Lab Chip* **22**, 2364 (2022).
- 38<sup>M.</sup> Rakhsha, C. E. Kees, and D. Negrut, “Lagrangian vs. Eulerian: An analysis of two solution methods for free-surface flows and fluid solid interaction problems,” *Fluids* **6**, 460 (2021).
- 39<sup>J.</sup> Feng, H. H. Hu, and D. D. Joseph, “Direct simulation of initial value problems for the motion of solid bodies in a Newtonian fluid Part 1. Sedimentation,” *J. Fluid Mech.* **261**, 95–134 (1994).
- 40<sup>J.</sup> Zhou and I. Papautsky, “Fundamentals of inertial focusing in microchannels,” *Lab Chip* **13**, 1121–1132 (2013).
- 41<sup>C.</sup> Prohm and H. Stark, “Feedback control of inertial microfluidics using axial control forces,” *Lab Chip* **14**, 2115–2123 (2014).
- 42<sup>C.</sup> Liu, G. Hu, X. Jiang, and J. Sun, “Inertial focusing of spherical particles in rectangular microchannels over a wide range of Reynolds numbers,” *Lab Chip* **15**, 1168–1177 (2015).
- 43<sup>F.</sup> P. Bretherton, “The motion of rigid particles in a shear flow at low Reynolds number,” *J. Fluid Mech.* **14**, 284–304 (1962).
- 44<sup>T.</sup> Zhang, H. Liu, K. Okano, T. Tang, K. Inoue, Y. Yamazaki, H. Kamikubo, A. K. Cain, Y. Tanaka, D. W. Inglis *et al.*, “Shape-based separation of drug-treated *Escherichia coli* using viscoelastic microfluidics,” *Lab Chip* **22**, 2801 (2022).
- 45<sup>M.</sup> Li, M. van Zee, K. Goda, and D. D. Carlo, “Size-based sorting of hydrogel droplets using inertial microfluidics,” *Lab Chip* **18**, 2575–2582 (2018).
- 46<sup>Z.</sup> Zhu, S. Li, D. Wu, H. Ren, C. Ni, C. Wang, N. Xiang, and Z. Ni, “High-throughput and label-free enrichment of malignant tumor cells and clusters from pleural and peritoneal effusions using inertial microfluidics,” *Lab Chip* **22**, 2097 (2022).
- 47<sup>D.</sup> Yuan, S. Yan, J. Zhang, R. M. Guijt, Q. Zhao, and W. Li, “Sheathless separation of *Cyanobacterial anabaena* by shape using viscoelastic microfluidics,” *Anal. Chem.* **93**, 12648 (2021).

- <sup>48</sup>M. Li, H. E. Muñoz, K. Goda, and D. D. Carlo, "Shape-based separation of microalga *Euglena gracilis* using inertial microfluidics," *Sci. Rep.* **7**, 10802 (2017).
- <sup>49</sup>P. Liu, H. Liu, D. Yuan, D. Jang, S. Yan, and M. Li, "Separation and enrichment of yeast *Saccharomyces cerevisiae* by shape using viscoelastic microfluidics," *Anal. Chem.* **93**, 1586 (2021).
- <sup>50</sup>H. Feng, M. Hockin, M. Capecchi, B. Gale, and H. Sant, "Size and shape based chromosome separation in the inertial focusing device," *Biomicrofluidics* **14**, 064109 (2020).
- <sup>51</sup>B. Behdani, S. Monjezi, M. J. Carey, C. G. Weldon, J. Zhang, C. Wang, and J. Park, "Shape-based separation of micro-/nanoparticles in liquid phases," *Biomicrofluidics* **12**, 051503 (2018).